Archived at the Flinders Academic Commons:

http://dspace.flinders.edu.au/dspace/

This is the publisher's copyrighted version of this article.

The original can be found at: http://www.agu.org/journals/jc/jc0503/2003JC002206/2003JC002206.pdf

© 2005 Journal of Geophysical Research

Published version of the paper reproduced here in accordance with the copyright policy of the publisher. Personal use of this material is permitted. However, permission to reprint/republish this material for advertising or promotional purposes or for creating new collective works for resale or redistribution to servers or lists, or to reuse any copyrighted component of this work in other works must be obtained from Journal of Geophysical Research.

Cyclogenesis in the deep ocean beneath Western Boundary Currents: A process-oriented numerical study

Jochen Kämpf

School of Chemistry, Physics and Earth Sciences, Flinders University of South Australia, Adelaide, South Australia, Australia

Received 16 November 2003; revised 21 October 2004; accepted 24 November 2004; published 1 March 2005.

[1] A two-layer shallow-water equation model is applied to a flat-bottom ocean on the f plane to explore instability mechanisms in Western Boundary Current (WBC) that lead to the formation of strong cyclones in the deep ocean underneath. Findings reveal a tight coupling of surface meandering and deep cyclogenesis, in agreement with observational evidence. Barotropic cyclones develop in timescales of 5–10 days and attain swirl speeds of >50 cm/s (depends on initial strength of WBC) on a diameter of ~100 km. Cyclogenesis is driven by advection of relative vorticity in the surface ocean and failure of the thermocline to respond rapidly enough to the associated sea level variations. Findings suggest that cyclogenesis and the associated strong abyssal flows (benthic storms) are ubiquitous features of WBCs and other frontal flows.

Citation: Kämpf, J. (2005), Cyclogenesis in the deep ocean beneath Western Boundary Currents: A process-oriented numerical study, *J. Geophys. Res.*, *110*, C03001, doi:10.1029/2003JC002206.

1. Introduction

[2] One of the primary scientific results of the Synoptic Ocean Prediction (SYNOP) observational program was the discovery of strong cyclones in the deep ocean beneath large-amplitude Gulf Stream meander troughs [*Johns et al.*, 1995; *Shay et al.*, 1995; *Watts et al.*, 1995; *Bower and Hogg*, 1996]. Strong abyssal flows (often referred to as benthic storms) have been observed before during High Energy Benthic Boundary Layer Experiment (HEBBLE) in the northwestern Atlantic [*Thomson and Luyten*, 1976; *Richards et al.*, 1981; *Nowell et al.*, 1982; *Welsh et al.*, 1991] and at other locations such as the western margin of the Greenland Sea [*Woodgate and Fahrbach*, 1999], in the Brazil Basin in the southwestern Atlantic [*Harkema and Weatherly*, 1996], and in the northeastern Atlantic [*Klein*, 1987]. Scientific findings from the SYNOP program, however, were the first that showed a close correlation between meanders of a Western Boundary Current (WBC) and strong cyclogenesis in the deep ocean underneath (Figure 1) [e.g., *Savidge and Bane*, 1999a, 1999b]. This provided a first detailed temporal and spatial coverage of benthic storm events and revealed the existence of strong barotropic cyclones in the deep sea attaining swirl speeds >0.5 m/s [*Savidge and Bane*, 1999a, 1999b]. These findings shed new light on instability mechanisms in WBCs, suggesting a tight coupling between barotropic and baroclinic dynamics, which currently is a field of intense oceanographic research. Cyclogenesis along WBCs appears to be a widespread phenomenon. Cyclonic meanders of the Agulhas Current, known as Natal Pulses, for instance, are believed to be instrumental in triggering the occlusion of an Agulhas Ring [e.g., *Lutjeharms et al.*, 2003].

[3] The SYNOP experiment revealed that deep cyclones develop quasi-stationary on timescales of 5–10 days, and that cyclone events are long-lived (typically lasting 6–9 weeks). Cyclones appear to be governed by quasi-geostrophic dynamics, associated with sea level anomalies of ~50 cm over a distance of ~50 km [*Savidge and Bane*, 1999a]. The radial structure and cyclone size (~50–100 km) does not change dramatically over the lifetime of an individual event. The cyclone size is ~3–5 times the Rossby radius of deformation of the first baroclinic mode, which is the fastest growing mode according to linear baroclinic instability theory [e.g., *Cushman-Roisin*, 1994]. During cyclone events, the thermocline structure beneath the Gulf Stream becomes distorted (see Figure 1), but it is not known whether this meandering triggers the cyclone or the other way around. On the basis of SYNOP field data, *Savidge and Bane* [1999b] compared the observed deep cyclogenesis with that in the atmosphere. They came to the conclusion that the ocean case did not resemble the atmospheric case, in that the ocean density field failed to account for the developing pressure centers. For unknown reasons, the observed anticyclones are typically far less energetic than cyclones (see Figure 1) and do not show much of an effect on the thermocline structure beneath the Gulf Stream.

[4] Although generation mechanisms of the cyclones are not fully understood, it is evident that they are driven by sea level variations, such that the divergence of mass transport in the upper ocean remains unbalanced by that in the deep ocean. *Savidge and Bane* [1999b] found that the production

Copyright 2005 by the American Geophysical Union.
0148-0227/05/2003JC002206$09.00

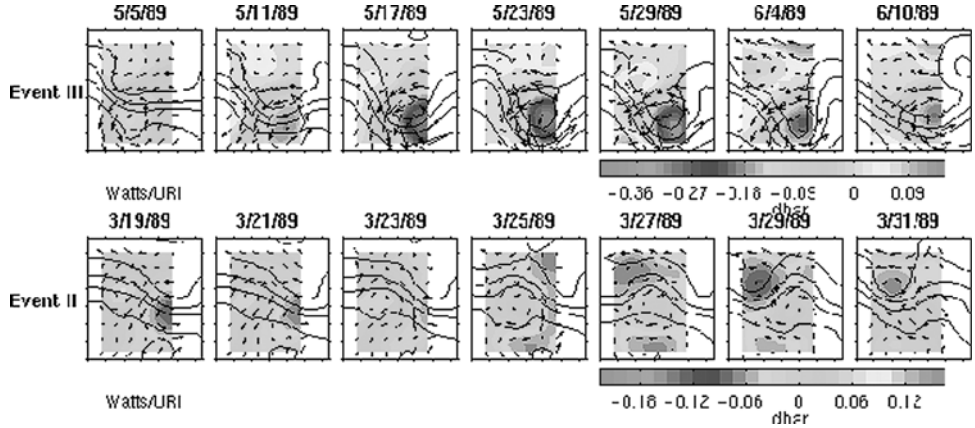

Figure 1. (top) Event III, cyclogenesis at a water depth of ~3.5 km beneath the Gulf Stream. Displayed are lateral distributions of pressure anomalies (shading), currents (arrows; maximum swirl speed ~25 cm/s), and depth contours of the 12°C thermocline (solid lines; CI = 200 m). The Gulf Stream runs from left to right, so that the thermocline depth decreases toward the top in each frame. Each frame covers an area of 200 km × 200 km. (bottom) Event II, development of a weak (swirl speed ~5 cm/s) anticyclone. Courtesy of Randy Watts (2003). See color version of this figure at back of this issue.

of relative vorticity in the lower layer (that is, the deep ocean from 700 m to ocean bottom) was primarily forced by water column stretching. In agreement with observational findings from *Howden* [1996], they also suggest that the production of relative velocity in the lower layer be directly related to the advection of relative vorticity in the upper layer. *Lindstrom et al.* [1997] have shown large vertical velocities at the thermocline during periods of Gulf Stream trough amplification and deep cyclogenesis. Values of 2–4 mm s^{-1} in the cyclone center, derived from temperature data and the heat equation, persisted for ~10 days or longer, and are in agreement with independent divergence estimates by *Savidge and Bane* [1999b]. Improvement of the understanding of the dynamics of WBCs and their instabilities is a primary task in oceanography and climate sciences for various reasons. For instance, case studies showed that baroclinic-barotropic interactions account for almost all of the eddy flux divergences and associated eddy-mean flow interactions [*Cronin and Watts*, 1996; *Cronin*, 1996] and therefore dominate in the meridional heat flux in the western Atlantic. These eddy fluxes need to be adequately represented in climate forecasting models. Moreover, a result of the predominance of cyclones and their quasi-stationary occurrence is the creation of a net circulation in the deep ocean. Annual averages reveal a westward flow in the northern portion of the SYNOP array, shoreward of the 4000-m isobath, running approximately parallel to topographic contours [*Watts et al.*, 2001] (see also D. R. Watts et al., Strong abyssal eddies coupled to the meandering Gulf Stream, 2001, available at http://www.po.gso.uri.edu/dynamics/wbc/WBCmain.html). This persistent flow (called "Slope Water Current") is presumably an important component of the Deep Western Boundary Current, a key player in the thermohaline circulation. Moreover, benthic storms are shown to be capable of resuspending and moving vast quantities of sediments [e.g., *Hollister and McCave*, 1984; *McCave*, 1986; *Hollister and Nowell*, 1991]. Hence knowledge of deep-sea sediment transport requires a detailed understanding of deep-ocean flows.

[5] As far as the author is aware, theories that comprehensively explain the observed cyclogenesis are lacking. The observed instability shows many features similar to those encountered in baroclinic instability [e.g., *Savidge and Bane*, 1999b]. However, previous studies have been either based on the reduced-gravity concept [e.g., *Griffiths et al.*, 1982; *Cushman-Roisin*, 1994; *Olascoaga and Ripa*, 1999; *Olascoaga*, 2001], which excludes flow in the deep ocean, or have used the rigid-lid approximation [e.g., *Reszka and Swaters*, 1999a, 1999b; *Karsten and Swaters*, 2000a, 2000b]. The rigid-lid approximation, however, removes the barotropic mode and implies that the ratio of upper layer to lower velocity scales is given by the reciprocal ratio of layer thicknesses [*Gill*, 1982] [see also *Reszka and Swaters*, 1999a, 1999b]. Hence "barotropic" stream functions predicted with rigid-lid models [e.g., *Karsten and Swaters*, 1999a, 1999b] are misleading, for they represent some depth-independent component of the flow rather than the true barotropic mode.

[6] This paper presents a numerical model that is a minimum requirement for the description of coupled barotropic-baroclinic instability mechanisms along WBCs. This model consists of a simple two-layer shallow-water equation model with freely moving sea surface and density interfaces (thermocline). This model is employed here in a process-oriented mode considering a highly simplified WBC for a flat-bottom ocean on the f plane. More confined, region-specific model applications (e.g., using realistic bathymetry for the Gulf Stream region) will be presented in subsequent publications.

2. Model

2.1. Governing Equations

[7] Mesoscale dynamics of the oceans (length scales ~100 km) can be described by the forced shallow-water equations [e.g., *Gill*, 1982] on the f plane. For simplicity, we treat a WBC as a depth-independent surface-ocean flow in a two-layer system on the f plane, as in the simple inertia

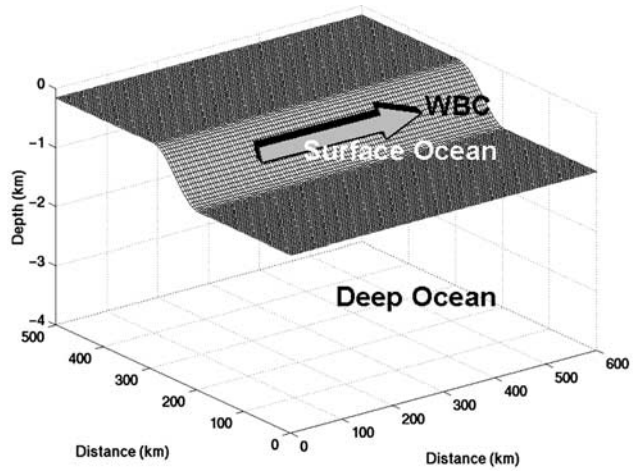

Figure 2. Model domain and thermocline structure used in this study.

theory of the Gulf Stream proposed by *Stommel* [1965]. Conservation of momentum and volume in the surface layer can then be formulated as

$$\frac{\partial u_1}{\partial t} + u_1\frac{\partial u_1}{\partial x} + v_1\frac{\partial u_1}{\partial y} - fv_1 = -g\frac{\partial \eta}{\partial x} + \frac{\partial u^*}{\partial t}, \tag{1a}$$

$$\frac{\partial v_1}{\partial t} + u_1\frac{\partial v_1}{\partial x} + v_1\frac{\partial v_1}{\partial y} + fu_1 = -g\frac{\partial \eta}{\partial y} + \frac{\partial v^*}{\partial t}, \tag{1b}$$

$$\frac{\partial \eta}{\partial t} + \frac{\partial[u_1(H_1+\eta)]}{\partial x} + \frac{\partial[v_1(H_1+\eta)]}{\partial y} = \frac{\partial h}{\partial t}, \tag{1c}$$

where x and y are horizontal Cartesian coordinates, t is time, u_1 and v_1 are horizontal flow components, $f \sim 10^{-4}$ s^{-1} is the Coriolis parameter (midlatitudes of Northern Hemisphere), g is acceleration due to gravity, η is sea surface elevation, H_1 is the undisturbed layer thickness, and h is the interface elevation. The perturbation velocities, u^* and v^*, are employed here to introduce initial small-amplitude disturbances to the flow. Lateral momentum diffusion was found insignificant (using a typical range of parameters) and has therefore been omitted.

[8] Conservation of momentum and volume in the deep-ocean layer can be formulated as

$$\frac{\partial u_2}{\partial t} + u_2\frac{\partial u_2}{\partial x} + v_2\frac{\partial u_2}{\partial y} - fv_2 = -\frac{\rho_1}{\rho_2}g\frac{\partial \eta}{\partial x} - \frac{\rho_2-\rho_1}{\rho_2}g\frac{\partial h}{\partial x} - ru_2\sqrt{u_2^2+v_2^2}/H_2, \tag{2a}$$

$$\frac{\partial v_2}{\partial t} + u_2\frac{\partial v_2}{\partial x} + v_2\frac{\partial v_2}{\partial y} + fu_2 = -\frac{\rho_1}{\rho_2}g\frac{\partial \eta}{\partial y} - \frac{\rho_2-\rho_1}{\rho_2}g\frac{\partial h}{\partial y} - rv_2\sqrt{u_2^2+v_2^2}/H_2, \tag{2b}$$

$$\frac{\partial h}{\partial t} + \frac{\partial[u_2(H_2+h)]}{\partial x} + \frac{\partial[v_2(H_2+h)]}{\partial y} = 0, \tag{2c}$$

where u_2 and v_2 are horizontal flow components, ρ_1 and ρ_2 are upper and lower layer densities, respectively, r is a bottom drag coefficient in a quadratic bottom friction approach, and H_2 is the undisturbed layer thickness. The bottom drag coefficient is chosen to be $r = 10^{-3}$. Bottom friction, however, was found to be insignificant and does not influence the results.

2.2. Numerical Techniques

[9] The algorithm used is straightforward. The governing equations are discretized on a rectangular, equally spaced Arakawa C-grid [*Arakawa and Lamb*, 1977] employing explicit Eulerian-forward time stepping. Bottom friction is implemented by a semi-implicit approach. Nonlinear terms are described by an upstream scheme. Time steps are limited by a Courant-number criterion that for two-dimensional flows takes the form

$$\Delta t \le \frac{\Delta x}{\sqrt{2gH_{\max}}}, \tag{3}$$

where Δt is the numerical time step, Δx is the grid spacing, and $H_{\max}$ is the maximum water depth encountered in the model domain.

2.3. Experimental Design

[10] The model domain has horizontal dimensions of 600 km $\times$ 500 km, resolved by a grid spacing of 5 km, and a total uniform water depth of 4000 m (Figure 2). A simplified WBC is assumed to run eastward (from left to right) across the model domain, as in Figure 1. Cyclic boundaries are implemented at the eastern and western margins of the domain, so that flows leaving a boundary enter through the opposite one. The model domain is chosen wide enough so that cyclic boundaries do not significantly influence the length scales of disturbances. Zero-gradient conditions are employed at the other boundaries.

[11] The control experiment considers a configuration that resembles that of the Gulf Stream. Upper and lower layer densities are chosen as ρ_1 = 1027 kg m^{-3} and ρ_2 = 1028 kg m^{-3}, respectively, and the density interface (thermocline) is assumed to vary by 800 m over a lateral distance of 100 km (Figures 2 and 3). This transition is described by means of a sinusoidal function. Initially, there is no motion in the bottom layer, which implies that baroclinic pressure gradients associated with the sloping thermocline cancel those imposed by the sloping sea surface. This condition, which is the basis of reduced-gravity models, is employed here exclusively to calculate the initial thermocline structure. Accordingly, the deep ocean is initially at rest. Fields of sea-surface elevation and interface displacement are then superimposed onto undisturbed layer thicknesses of H_1 = 600 m and H_2 = 3400 m, so that the thickness of the surface ocean varies between 200 m and 1000 m across the WBC. The geostrophic balance is used to calculate the initial flow in the upper layer. The structure of this flow is of cosine shape with peak speeds $\sim$1 m/s centered along regions of greatest sea-level slope.

[12] The total simulation time is 30 days resolved by time steps of 10 s. Small initial disturbances are introduced to facilitate the onset of dynamic instabilities. Ambient disturbances such as topographic Rossby waves could act to generate such initial perturbations. For the sake of this simplistic model application, however, any complex nonlocal dynamical influences are ignored. Instead of this, initial perturbations are artificially created by wind-stress forcing

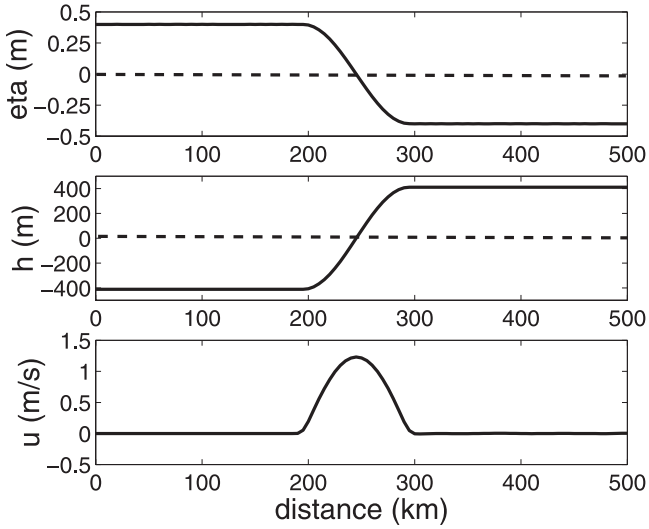

Figure 3. Initial conditions. (top) Sea-surface elevation (m) across a Western Boundary Current. (middle) Thermocline-depth variations (m) on the basis of the reduced-gravity concept. (bottom) Geostrophic flow speed (m/s) of the surface-ocean flow. Note that the coast along WBCs is located on the shallow side of the surface layer, that is, to the right in the above frames.

in terms of a wind pattern (100 km in diameter) that decays away during the first 5 days of simulation, that is, well before the WBC becomes noticeably unstable. Note that experiments without such initial wind-generated disturbances but with some extra noise (<1 m per 5 km) added to the bottom topography yielded similar results.

[13] The temporal evolution of instabilities is monitored by means of layer-averaged kinetic and available potential energies. The total energy in a two-layer flow is given by [e.g., *Gill*, 1982]

$$TE = KE1 + KE2 + APE1 + APE2. \tag{4}$$

Kinetic energies in surface and bottom layers are given by

$$KE1 = \int\int \left\{ \frac{1}{2}\rho_1 \sqrt{u_1^2 + v_1^2}(H_1 + \eta - h) \right\} \mathrm{dxdy} \tag{5a}$$

$$KE2 = \int\int \left\{ \frac{1}{2}\rho_2 \sqrt{u_2^2 + v_2^2}(H_2 + h) \right\} \mathrm{dxdy}. \tag{5b}$$

Available potential energies associated with sea level variations and thermocline displacements, respectively, are given by

$$APE1 = \int\int \left\{ \frac{1}{2}\rho_1 g \eta^2 \right\} \mathrm{dxdy} \tag{6a}$$

$$APE2 = \int\int \left\{ \frac{1}{2}(\rho_2 - \rho_1) g h^2 \right\} \mathrm{dxdy}. \tag{6b}$$

3. Results and Discussion

3.1. Energy Considerations

[14] Figure 4 displays evolutions of layer-averaged kinetic and available potential energies (per unit surface). Disturbances start to grow after 10 days of simulation and approach steady-state energy levels after ~20 days. During this growth phase, the kinetic energy in both layers increases to approach approximately the same final value ($\sim 8 \times 10^4$ J/m^2) after 20 days and onward. This reflects the highly barotropic nature of the resultant flows. Notice that the rate of increase in kinetic energy in the deep ocean is steeper than that in the surface ocean. This increase is provided mostly by the potential energy of the density stratification, similar to energy conversions in classical baroclinic instability. Notice that there is also some decrease in available potential energy in the surface layer associated with initial sea level anomalies. After 30 days, ~35% of the initial total energy has dissipated, 50% is still being stored in the density stratification, and 15% has been converted into kinetic energy to create strong deep-ocean flow of speeds >50 cm/s (Figure 5). Notice the slight changes of

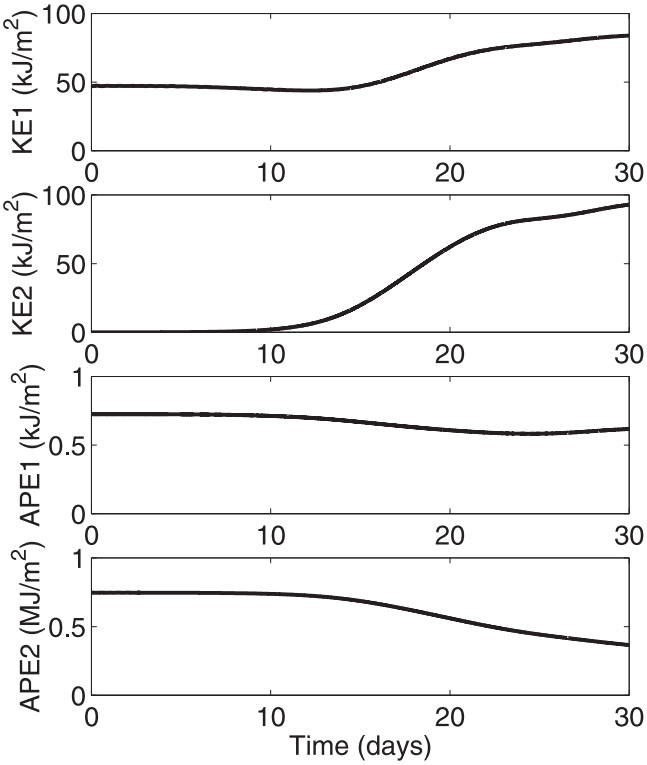

Figure 4. Evolutions of kinetic energy and available potential energy per unit surface (see text for definition of individual terms).

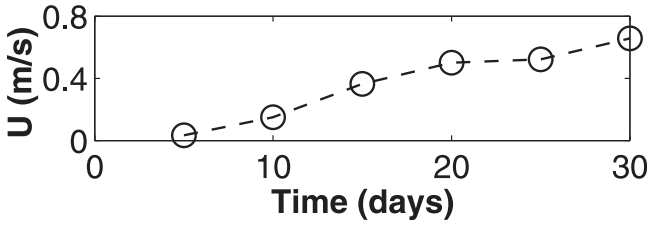

Figure 5. Evolution of swirl speed (m/s) of barotropic cyclones.

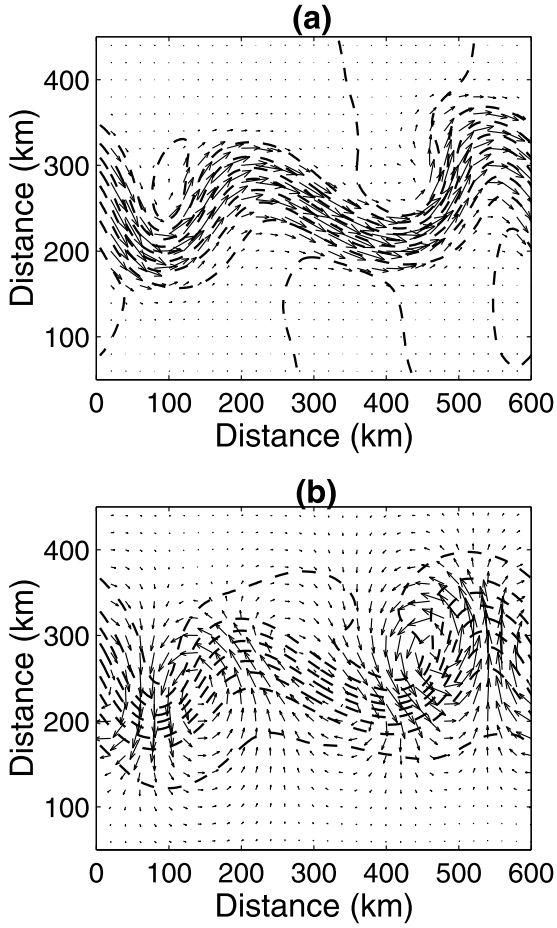

Figure 6. Lateral distributions at day 15. (a) Sea level contours (broken lines; CI = 0.1 m) and horizontal flow vectors in the surface layer (arrows, maximum speed is 1.2 m/s). (b) Interface displacement (broken lines; CI = 100 m) and horizontal flow vectors in the bottom layer (arrows, maximum speed is 0.35 m/s). Every fifth data point is shown in the vector fields.

energy levels and flow speeds after day 25. These changes are associated with cyclones, spinning off from the WBC and interfering with the boundaries (see Figure 14 in section 3.7).

3.2. Surface and Interface Displacements and Barotropic Dynamic Topography

[15] In the following, the focus is placed into the early growth phase of disturbances by exploring snapshots of lateral distributions at day 15. By this day, the surface flow has already created meanders on a wavelength of ~200 km (Figure 6a) while remaining largely in a geostrophic balance. This meandering is accompanied by the creation of cyclonic mesoscale eddies in the deep ocean of ~100 km in diameter (Figure 6b). At day 15 the swirl speed of cyclones already exceeds 30 cm/s, strengthening to >50 cm/s during the subsequent 10 days (see Figure 5). Along its trajectories, the deep ocean flow experiences significant variations in layer thickness (~800 m), and this feature is strongest near troughs and crests of surface meanders. The thermocline is a mirror of surface meanders and gradually deepens under meander troughs. Directions between surface-ocean and deep-ocean flows differ locally considerably by up to 90°. The surface flow cannot be described as a linear superposition of initial flow and the evolving barotropic flow. Instead of this, the barotropic flow interacts with the baroclinic flow via the nonlinear terms, so that meanders also appear in the baroclinic flow component (not shown). Simulated abyssal flow field and thermocline structure are in excellent qualitative and quantitative agreement with field observations (see Figure 1) [*Savidge and Bane*, 1999a, 1999b].

[16] Deep-ocean flow is driven by horizontal pressure gradients due to slopes in sea level and thermocline depth. The resultant dynamic pressure is proportional to a "barotropic dynamic topography," given by

$$BDT = -\frac{\rho_1}{\rho_2}\eta - \frac{\rho_2 - \rho_1}{\rho_2}h. \tag{7}$$

Pressure forcing in the deep ocean vanishes if this barotropic dynamic topography is zero everywhere, which is the basis of the reduced-gravity concept. Figure 7 shows that this is not the case here. Instead of this, low-pressure cells develop in the deep ocean to drive strong quasi-geostrophic abyssal flow. At day 15, low-pressure anomalies correspond to an equivalent sea-level anomaly of −10 cm, increasing in magnitude to −20 cm afterward. The simulated deep-ocean pressure distributions agree well with those observed in the SYNOP experiment (see Figure 1). Low-pressure cells are located between a meander trough and the adjacent crest (in a downstream sense), whereas there are only weak anticyclones forming between crests and troughs, in consistency with the field observations (see Figure 1).

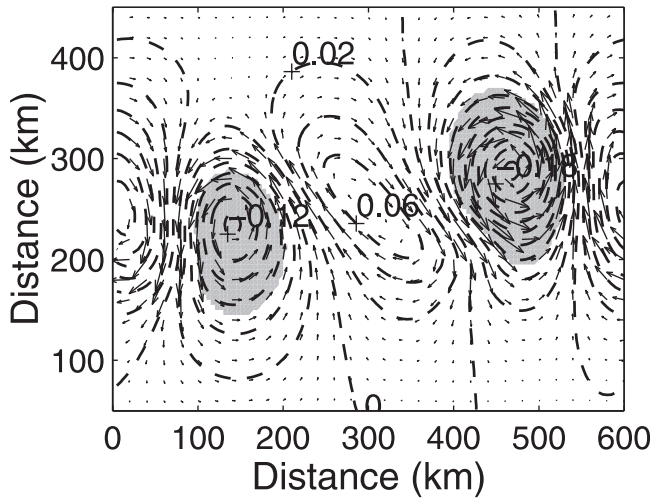

Figure 7. Lateral distribution of barotropic dynamic topography (broken lines; CI = 0.02 m) at day 15. Shaded areas highlight values <−0.05 cm. Deep-ocean flow vectors (arrows; every fifth data point; maximum speed is 0.2 m/s) are superimposed.

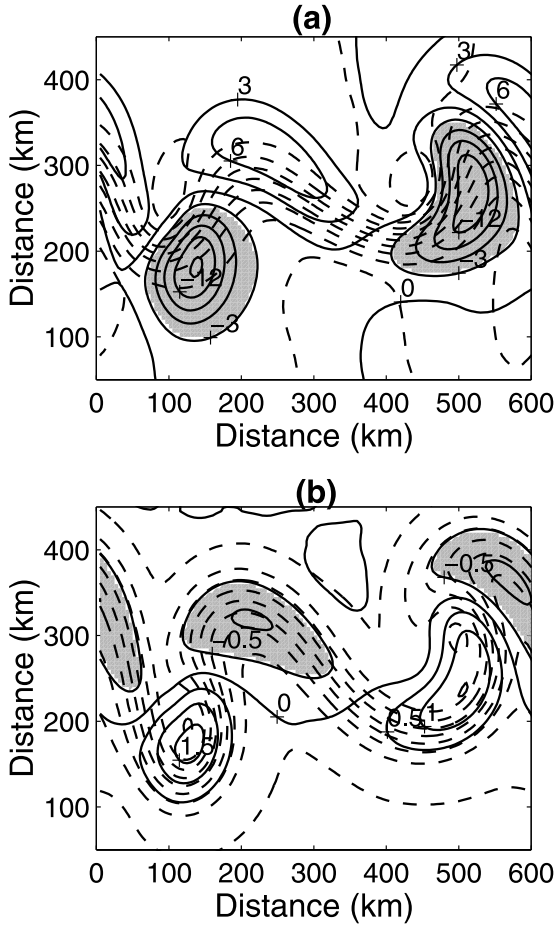

Figure 8. (a) Lateral distributions of vertical displacement speeds of the sea surface (solid lines; CI = 3 cm/day). Shaded areas highlight values <−3 cm/day. Sea-level contours from day 15 (broken lines; CI = 0.1 m) are superimposed. (b) Lateral distributions of vertical displacement speeds of the thermocline (solid lines; CI = 0.5 mm/s ≈ 43 m/day). Shaded areas highlight values <−0.5 mm/s. Contours of interface displacement from day 15 (broken lines; CI = 100 m) are superimposed. Trends are derived from the difference of values between day 20 and day 15.

3.3. Pressure Tendency and Vertical Displacement Speeds

[17] The pressure tendency in the deep ocean depends on the parallel evolutions of sea surface and thermocline depth. Thermocline depth evolves according to

$$\frac{\partial h}{\partial t} = -\left[u_2 \frac{\partial (H_2 + h)}{\partial x} + v_2 \frac{\partial (H_2 + h)}{\partial y}\right] - \left[(H_2 + h)\left(\frac{\partial u_2}{\partial x} + \frac{\partial v_2}{\partial y}\right)\right], \quad (8)$$

in response to (1) water-column stretching/shortening in flows experiencing a spatial variation in layer thickness (first-bracket terms) and (2) the local effect of diverging or converging currents (second-bracket terms). Hereinafter the second term is referred to as flow convergence (or flow divergence) if it corresponds to a positive (or negative) vertical displacement of the thermocline. The effect of flow divergence in the deep ocean is less pronounced compared with water-column stretching and there is a lag of approximately a quarter wavelength between these patterns (not shown). The resultant vertical displacement speed of the thermocline is ∼2 mm/s (∼170 m/day) below meander troughs, in agreement with the measurements of *Lindstrom et al.* [1997], and −1 mm/s below meander crests (Figure 8b). Upward displacement speeds exceed downward speeds, so that cyclones grow at a faster rate than anticyclones, in agreement with SYNOP observations. Reasons for this cyclonic preference are given in Appendix A.

[18] Sea level changes follow the volume conservation equation for the surface layer; that is,

$$\frac{\partial \eta}{\partial t} = -\left[u_1 \frac{\partial (H_1 + \eta)}{\partial x} + v_1 \frac{\partial (H_1 + \eta)}{\partial y}\right] - \left[(H_1 + \eta)\left(\frac{\partial u_1}{\partial x} + \frac{\partial v_1}{\partial y}\right)\right] + \frac{\partial h}{\partial t}, \quad (9)$$

that in addition to water-column stretching and flow divergence, also contains the net rate of change of thermocline depth. In the surface layer, as in the bottom layer, water-column stretching dominates over flow divergence (not shown). However, the effects of water-column stretching and flow divergence are anticorrelated between the layers, so that it is a slight imbalance of the distributions that makes up the resultant sea-level change. This slight but systematic imbalance arises mainly from enhanced nonlinear effects in the surface layer associated with a curvature of the baroclinic flow component (not shown). The net result of this imbalance is differential vertical displacement speeds of the sea surface of −10 cm/day at meander troughs and 6 cm/day in the vicinity of meander crests (Figure 8a). This process resembles that described by linear baroclinic instability theory [see *Cushman-Roisin*, 1994] with the slight difference that the latter neglects the barotropic mode and, owing to linearization, does not distinguish between cyclone and anticyclone development (see Appendix A).

3.4. Failure of Baroclinic Compensation

[19] Vertical displacement speeds of the sea surface are much smaller (∼150 times smaller) than those of the thermocline (see Figure 8), but nevertheless large enough to support cyclogenesis in the deep ocean. Vertical displacements of the sea surface are opposed to those of the thermocline, so that there is a tendency of the thermocline to baroclinically compensate for sea-level variations. In general, this baroclinic compensation process operates to weaken the deep-ocean flow. Perfect baroclinic compensation corresponding to vanishing deep-ocean flow would require a ratio of displacement speeds of

$$-\frac{\partial h/\partial t}{\partial \eta/\partial t} = \frac{\rho_2}{\rho_2 - \rho_1} \sim 1000. \quad (10)$$

The predicted (negative) ratio of vertical displacement speeds between the sea surface and the thermocline is much smaller (∼200), so that clearly the thermocline fails to respond rapidly enough to sea-level variations. Accordingly,

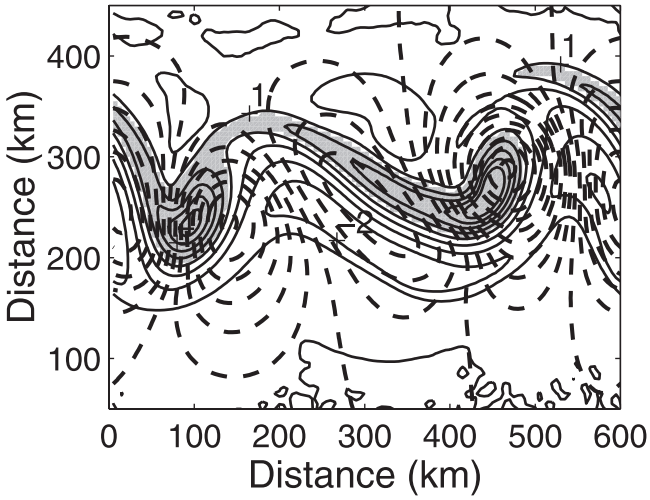

Figure 9. Lateral distribution of relative vorticity in the surface layer (solid lines; CI = 1×10^{-5} s^{-1}) at day 15. Shaded areas highlight values $>1 \times 10^{-5}$ s^{-1}. Contours of barotropic dynamic topography (broken lines; CI = 0.02 m) are superimposed.

there is a failure of baroclinic compensation, which implies that the barotropic mode of instabilities intensifies with time. Hence, meandering of the surface flow and cyclogenesis are the signature of the same instability process.

3.5. Vorticity Considerations

[20] The vorticity tendency equation in each layer is given by

$$\frac{\partial \varsigma}{\partial t} = -f\left(\frac{\partial u}{\partial x} + \frac{\partial v}{\partial x}\right) - u\frac{\partial \varsigma}{\partial x} - v\frac{\partial \varsigma}{\partial y}, \tag{11}$$

where $\zeta = (\partial v/\partial x - \partial u/\partial y)$ is the relative vorticity. Scaling considerations (confirmed by case studies) have shown that frictional effects are insignificant and therefore can be omitted. Relation (11) expresses that relative vorticity varies temporally in response to (1) divergence of horizontal flow, which can only come from ageostrophic currents, and (2) vorticity advection, which is dominated by the geostrophic flow. Initially, the surface-ocean frontal flow exhibits positive (cyclonic) relative vorticity along its shallow portion and negative (anticyclonic) relative vorticity along the deeper portion. This main structure is still maintained to some degree at day 15 (Figure 9), but there is superimposed the clear signature of mesoscale cyclones (being stronger than anticyclones) that increase the relative vorticity in the vicinity of meander troughs to values of 5×10^{-5} s^{-1}. Note that this is about half the planetary vorticity (1×10^{-4} s^{-1}). The relative vorticity of cyclones intensifies with time at rates of up to 2×10^{-6} s^{-1} per day (Figure 10). The source of this strengthening is advection of relative vorticity (Figure 11a)

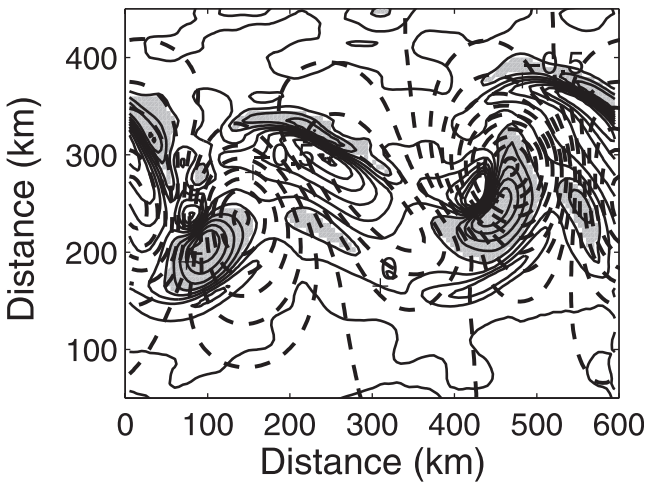

Figure 10. Lateral distribution of net vorticity tendency in the surface layer (solid lines; CI = 0.5×10^{-10} s^{-2}) at day 15. Shaded areas show values $>0.5 \times 10^{-10}$ s^{-2}. Contours of barotropic dynamic topography (broken lines; CI = 0.02 m) are superimposed.

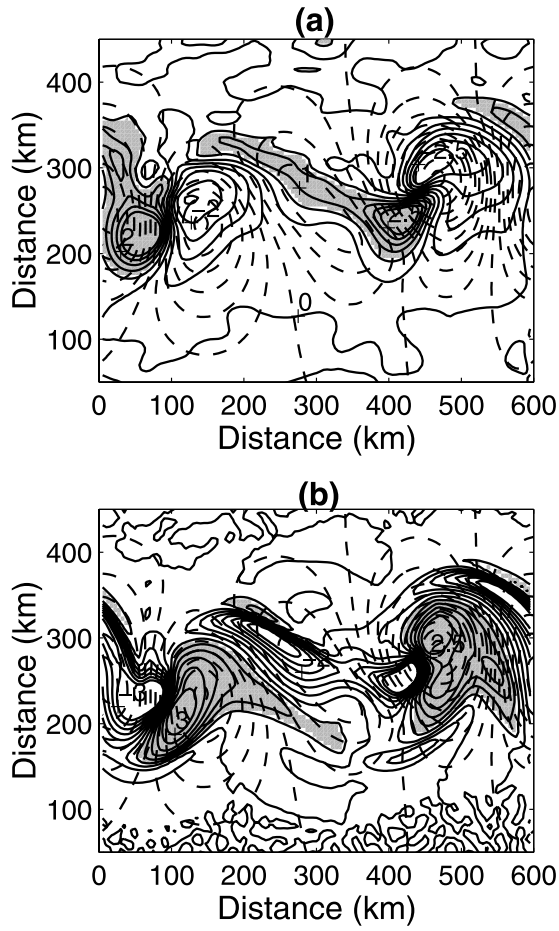

Figure 11. (a) Lateral distributions in the surface layer at day 15 of vorticity tendency due to divergence of ageostrophic flow (solid lines; CI = 0.5×10^{-10} s^{-2}). Shaded areas highlight values $>0.5 \times 10^{-10}$ s^{-2}. (b) Lateral distributions in the surface layer at day 15 of vorticity tendency due to advection of relative vorticity (solid lines; CI = 0.5×10^{-10} s^{-2}). Shaded areas highlight values $>0.5 \times 10^{-10}$ s^{-2}. Contours of barotropic dynamic topography (broken lines; CI = 0.02 m) are superimposed.

that overcomes the dampening effect of convergence in the ageostrophic flow (Figure 11b), in agreement with the analysis of *Howden* [1996].

[21] The relative vorticity pattern in the deep ocean displays the existence of cyclones at meander troughs (Figure 12). The magnitude of relative vorticity in these cyclones is $\sim 1 \times 10^{-5}$ s^{-1}. Cyclones strengthen at a rate of $\sim 2 \times 10^{-7}$ s^{-1} per day (Figure 13a), which is mainly caused by divergence of the ageostrophic flow (Figure 13b); that is, advection of relative vorticity is negligibly small in the bottom layer (not shown). Hence, in agreement with observational evidence [e.g., *Savidge and Bane*, 1999b] and previous considerations [e.g., *Bjerknes and Holmboe*, 1944], we find that cyclogenesis is directly associated with advection of relative vorticity in the upper ocean and vortex-tube stretching in the deep ocean.

3.6. Comparison With Previous Studies

[22] According to linear baroclinic instability theory adopted for a two-layer ocean [*Pedlosky*, 1987], baroclinic disturbances become unstable and grow if their wavelength exceeds

$$\lambda > \pi f^{-1} \left[g \frac{\Delta \rho}{\rho_o} (h_1 h_2)^{1/2} \right]^{1/2}, \qquad (12)$$

where h_1 and h_2 are upper and lower layer thicknesses along the frontal zone. For parameters used in this study, (12) gives $\lambda > 100$ km, which is in excellent agreement with our results (see Figure 6). In our study, growth of disturbances takes place between day 15 and day 20, giving an e-folding timescale of $\sim$5 days that corresponds to a growth rate of 0.1 f, which is in good agreement with previous studies [see *Eldevik*, 2002]. The barotropic disturbances, described in this paper, attain length scales and growth rates similar to those encountered in the classical baroclinic instability process. Appendix A discusses the preference of cyclones over anticyclones.

3.7. Other Features

[23] The swirl speed of abyssal cyclones increases to values of $\sim$50 cm/s (see Figure 5). A sequence of case studies in which the initial strength of the WBC has been varied (not shown) suggests that the swirl speed of abyssal cyclones be about half the "ambient" frontal speed of the WBC. This indicates that exclusively swift boundary currents, such as the Gulf Stream, can produce energetic abyssal flows.

[24] In all the simulations we have conducted, there was a point in time at which cyclones spun up from the frontal flow (see Figure 14) and, indeed, became influenced by boundary conditions. For instance, this happened after day 25 in the simulation discussed above (see Figures 4 and 5). Boundary conditions, however, had no impact on the energetics and spatial scales of disturbances during the

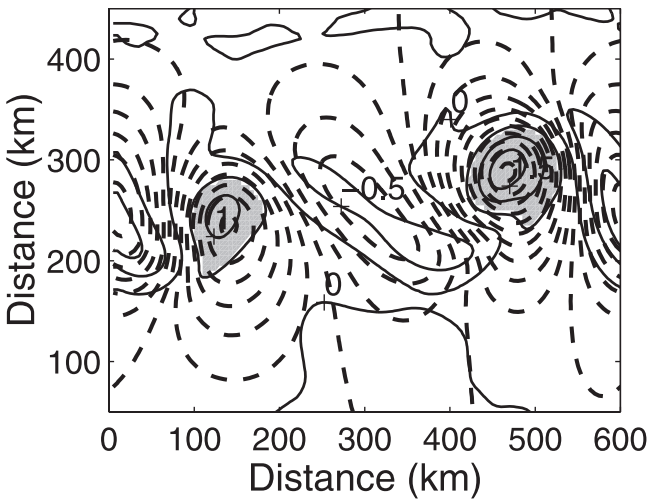

Figure 12. Lateral distribution of relative vorticity in the bottom layer (solid lines; CI = 0.5 $\times$ 10^{-5} s^{-1}) at day 15. Shaded areas highlight values >0.5 $\times$ 10^{-5} s^{-1}. Contours of barotropic dynamic topography (broken lines; CI = 0.02 m) are superimposed.

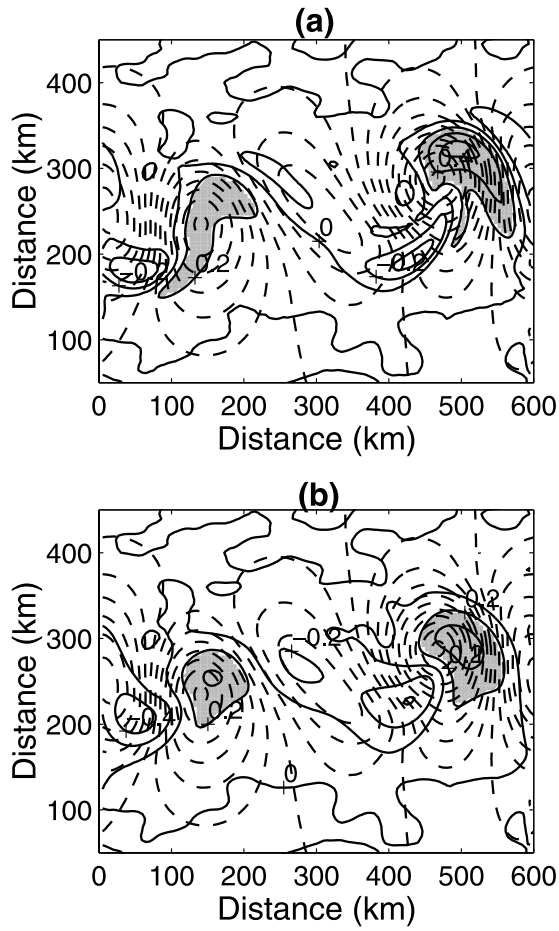

Figure 13. (a) Lateral distributions in the bottom layer at day 15 of net vorticity tendency (solid lines; CI = 0.2 $\times$ 10^{-10} s^{-2}). Shaded areas highlight values >0.2 $\times$ 10^{-10} s^{-2}. (b) Lateral distributions in the bottom layer at day 15 of vorticity tendency due to divergence of ageostrophic flow (solid lines; CI = 0.2$\times$10^{-10} s^{-2}). Shaded areas highlight values >0.2 $\times$ 10^{-10} s^{-2}. Contours of barotropic dynamic topography (broken lines; CI = 0.02 m) are superimposed.

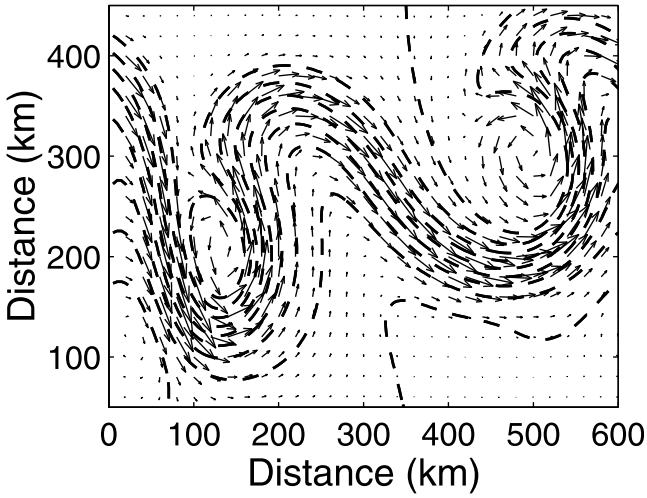

Figure 14. Lateral distributions of sea-level elevation (broken lines; CI = 0.1 m) and horizontal flow vectors in the surface layer (arrows, maximum speed is 1.2 m/s) at day 20. Every fifth data point is shown in the vector fields.

initial growth phase (from days 10 to 20), as being verified in comparison studies (not shown).

4. Conclusions

[25] This paper employs a two-layer shallow-water equation model to explore dynamic instabilities in an idealized Western Boundary Current (WBC) for a flat-bottom ocean on the f plane. The important difference between this approach with previous theoretical studies is the use of a freely moving sea surface, which retains the barotropic mode. Findings are in striking agreement with SYNOP observational evidence in terms of growth rates, swirl speeds, and spatial scales of mesoscale cyclones evolving. This indicates that the model captures the key elements of the instability process. Moreover, it is revealed that meandering of a WBC and cyclogenesis in the deep ocean underneath are indistinguishable parts of the same instability process. Hence benthic storm events can be predicted by means of monitoring the surface appearance of a WBC from satellite-derived data (e.g., SST, altimetric sea level, ocean color). In agreement with previous observational findings [*Savidge and Bane*, 1999b], this study suggests that advection of relative vorticity in the surface ocean triggers deep cyclogenesis by means of vortex-tube stretching. There is a resemblance of this barotropic-baroclinic instability mechanism to that described in baroclinic instability theory. Apart from similar growth rates and wavelengths, as discussed above, the upper layer pressure field also tends to lag the lower layer pressure field by a quarter wavelength (see Figure 6), which is a typical feature inherent with baroclinic instabilities. Nevertheless, baroclinic theories that employ a rigid-lid approximation cannot adequately describe cyclogenesis in the deep ocean as they significantly underestimate the magnitude of the deep-ocean flow. Further theoretical work is thus required to enhance understanding of deep cyclogenesis in the oceans.

[26] This paper focuses more on the initial perturbation phase rather than on instances when meanders pinch off from the WBC to form rings. A larger model domain and longer simulation times than considered here are required to explore the fate of deep cyclones beneath fully developed rings. Moreover, the SYNOP array results show that the cyclogenesis process is far more variable and unpredictable than captured by this model application. A reason of this might be nonlocal effects (such as topographic Rossby waves) that can operate to modify local meanders by triggering either growth or decay depending on phasing of resulting convergences and divergences.

[27] Many interesting questions remain that could not be addressed by this paper. What is the effect of variable bottom topography? How does the residual (time-averaged) deep flow interact with the larger-scale deep circulation? What happens in a WBC that produces mainly anticyclones such as the East Australian Current? How does deep cyclogenesis influence the dynamics of circumpolar currents such as the Antarctic Circumpolar Current? What role does cyclogenesis play in coastal density fronts such as the Antarctic Slope Front? What is the associated sediment resuspension rates and lateral transport? Although these

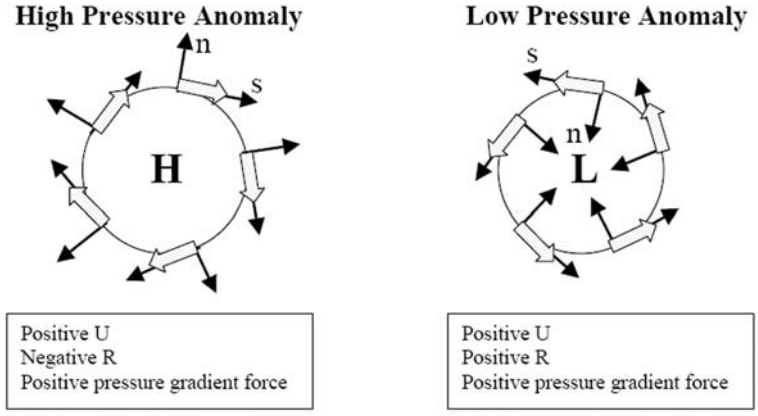

Figure A1. Sketch of the movement of fluid parcels around (left) high-pressure and (right) low-pressure anomalies in local coordinates (s,n). See text.

equations could not be addressed, this study provides significant new insights into the nature of cyclogenesis in the deep sea and forms a firm basis for future research, both theoretical and observational.

Appendix A: Cyclonic Preference

[28] Cyclonic lows dominate the baroclinic flow that constitutes the synoptic weather. The atmospheric literature is rich in papers demonstrating cyclogenesis [e.g., *Bjerknes and Holmboe*, 1944] with *Garnier et al.* [1998] as a recent example. In oceanic literature, a dominance of cyclones is found by *Wang* [1993], *Samelson and Chapman* [1995], and *Eldevik and Dysthe* [2002]. To the belief of the author, the easiest way to understand this cyclonic preference, which seems to be common in both the atmosphere and the oceans, is to examine the gradient-wind equations [e.g., *Shaw*, 1908; *Rossby*, 1940; *Gill*, 1982]. To this end, local coordinates on the horizontal plane are employed whereby the coordinate s is tangential to the particle path and the coordinate n is normal to this (see Figure A1). Then, the quasi-geostrophic momentum equation normal to the particle path can be written as [e.g., *Gill*, 1982, p. 235]

$$U^2/R + fU = -\rho_o^{-1}\partial P/\partial n, \tag{A1}$$

where R is the radius of curvature, which is positive(negative) if it is measured along positive (negative) s coordinate (see Figure A1). The first term in (A1) is a centrifugal acceleration term that operates to deflect the path from geostrophic streamlines owing to inertia effects. This ageostrophic effect becomes stronger with increasing curvature; that is, with decreasing magnitude of the radius of curvature. The resulting pathway for a radial symmetric pressure field is a spiral. It is believed that this spiralling effect during atmospheric cyclogenesis triggers so-called spiral eddies frequently seen at the ocean surface [e.g., *Munk et al.*, 2000].

[29] For both cyclones and anticyclones the centrifugal acceleration is directed radially away from the pressure center (Figure A1) and aims at making trajectories straighter. As a result of this, there is net flow divergence (caused by all particles that spiral around a mesoscale pressure anomaly) that operates to lower the pressure anomaly. This intensifies cyclones, but weakens anticyclones.

[30] It is useful to inspect solutions of (A1) for a given, frozen horizontal pressure-gradient field. Note that solutions must satisfy the condition $U \geq 0$. For a cyclonic pressure field ($R > 0$), the solution reads

$$U_{cyclone} = 0.5fR\left(\sqrt{1+a} - 1\right), \tag{A2}$$

where the "parameter" a is given by

$$a = -4\rho_o^{-1}\partial P/\partial n\left(f^2R\right)^{-1}, \tag{A3}$$

which is positive for the cyclonic case. According to this solution, U has a lower limit of zero but there is no mathematical upper limit. As curvature of particle trajectories becomes stronger during the baroclinic instability process, so does the centrifugal acceleration term. In other words, nonlinear terms become increasingly significant, so that the flow becomes more and more ageostrophic. In cyclones, this enhancement of ageostrophic effects goes hand in hand with an intensification of the pressure anomaly (resulting from net flow divergence). Hence the magnitude of a increases with time, and so does the swirl speed (A3). Accordingly, both ageostrophic and geostrophic flow components in cyclones grow simultaneously with time.

[31] For an anticyclonic pressure field ($R < 0$), on the other hand, there are two positive roots of equation (A1). Only one of these roots, that is,

$$U_{anticyclone} = 0.5f|R|\left(1 + \sqrt{1-|a|}\right), \tag{A4}$$

is physically plausible, for it converges into the inertia radius relationship for vanishing pressure gradients. Thus, U is always in a range between $0.5\,f|R|$and $f|R|$, which relates to the condition

$$|a| < 1 \Rightarrow -\rho_o^{-1}\partial P/\partial n < 0.25f^2|R|. \tag{A5}$$

Here, as the curvature of particle trajectories becomes stronger, there is a weakening of the pressure anomaly owing to flow divergence and the process converges into a pure inertial oscillation void of lateral pressure gradients.

[32] Topographic effects, not considered in this study, influence the baroclinic instability process and can in certain circumstances support the generation of anticyclones. An example of this is flows around mountains (or seamounts), known as Taylor columns, which are generally anticyclonic owing to a flow convergence.

[33] **Acknowledgment.** The author is grateful for the fruitful comments of two referees that significantly improved this work that was supported by a research grant funded by Flinders University, Australia.

References

Arakawa, A., and V. R. Lamb (1977), Computational design of the basic dynamical processes of the UCLA General Circulation Model, *Methods Computat. Phys.*, *17*, 174–267.

Bjerknes, J., and J. Holmboe (1944), On the theory of cyclones, *J. Meteorol.*, *1*, 1–22.

Bower, A. S., and N. G. Hogg (1996), The structure of the Gulf Stream and its recirculation at 55°W, *J. Phys. Oceanogr.*, *26*, 1002–1022.

Cronin, M. (1996), Eddy-mean flow interaction in the Gulf Stream at 68°W: Part II. Eddy forcing on the time-mean flow, *J. Phys. Oceanogr.*, *26*, 2132–2151.

Cronin, M., and D. R. Watts (1996), Eddy-mean flow interaction in the Gulf Stream at 68°W: Part I. Eddy energetics, *J. Phys. Oceanogr.*, *26*, 2107–2131.

Cushman-Roisin, B. (1994), *Introduction to Geophysical Fluid Dynamics*, 320 pp., Prentice-Hall, Upper Saddle River, N. J.

Eldevik, T. (2002), On frontal dynamics in two model oceans, *J. Phys. Oceanogr.*, *32*, 2915–2925.

Eldevik, T., and K. B. Dysthe (2002), Spiral eddies, *J. Phys. Oceanogr.*, *32*, 851–869.

Garnier, E., O. Métais, and M. Lesieur (1998), Synoptic and frontal-cyclone scale instabilities in baroclinic jet flows, *J. Atmos. Sci.*, *55*, 1316–1335.

Gill, A. E. (1982), *Atmosphere-Ocean Dynamics*, *Int. Geophys. Ser.*, vol. 30, 626 pp., Academic, San Diego, Calif.

Griffiths, R. W., P. D. Killworth, and M. E. Stern (1982), Ageostrophic instability of ocean currents, *J. Fluid Mech.*, *117*, 343–377.

Harkema, R., and G. L. Weatherly (1996), A compilation of moored current meter data from the southern boundary of the Brazil basin for the deep basin experiment September 1993–March 1995, *Tech. Rep. CMF-96-01*, Florida State Univ., Tallahassee.

Hollister, C. D., and I. N. McCave (1984), Sedimentation under deep-see storms, *Nature*, *309*, 220–225.
Hollister, C. D., and A. R. M. Nowell (1991), HEBBLE epilogue, *Mar. Geol.*, *99*, 445–460.
Howden, S. D. (1996), Processes associated with steep meander development in the Gulf Stream near 68°W, Ph.D. thesis, 229 pp., Univ. of R. I., Kingston.
Johns, W. E., T. J. Shay, J. M. Bane, and D. R. Watts (1995), Gulf Stream structure, transport, and recirculation near 68°W, *J. Geophys. Res.*, *100*, 817–838.
Karsten, R. H., and G. E. Swaters (2000a), Nonlinear effects in two-layer, large-amplitude, geostrophic dynamics: Part 2. The weak-beta case, *J. Fluid Mech.*, *412*, 160–196.
Karsten, R. H., and G. E. Swaters (2000b), Nonlinear effects in two-layer, large-amplitude, geostrophic dynamics: Part 1. The strong-beta case, *J. Fluid Mech.*, *412*, 125–160.
Klein, H. (1987), Benthic storms, vortices and particle dispersion in the Deep West European Basin, *Dtsch. Hydrol. Z.*, *49*, 87–102.
Lindstrom, S., X. Qian, and D. R. Watts (1997), Vertical motion in the Gulf Stream and its relation to meanders, *J. Geophys. Res.*, *102*, 8485–8503.
Lutjeharms, J. R. E., O. Boebel, and H. T. Rossby (2003), Agulhas cyclones, *Deep Sea Res., Part II*, *50*, 13–34.
McCave, I. N. (1986), Local and global aspects of the bottom nepheloid layers in the world Ocean, *Neth. J. Sea. Res.*, *20*, 167–181.
Munk, W., L. Armi, K. Fischer, and F. Zachariasen (2000), Spirals on the sea, *Proc. R. Soc. London, Ser. A*, *456*, 1217–1280.
Nowell, A. R. M., C. D. Hollister, and P. A. Jumars (1982), High energy benthic boundary layer experiment: HEBBLE, *Eos Trans. AGU*, *63*(31), 594–595.
Olascoaga, M. J. (2001), Deep ocean influence on upper ocean baroclinic instability, *J. Geophys. Res.*, *106*, 26,863–26,877.
Olascoaga, M. J., and P. Ripa (1999), Baroclinic instability in a two-layer model with a free boundary and β effect, *J. Geophys. Res.*, *104*, 23,357–23,366.
Pedlosky, J. (1987), *Geophysical Fluid Dynamics*, 2nd ed., 710 pp., Springer-Verlag, New York.
Reszka, M. K., and G. E. Swaters (1999a), Eddy formation and interaction in a baroclinic frontal geostrophic model, *J. Phys. Oceanogr.*, *29*, 3025–3042.
Reszka, M. K., and G. E. Swaters (1999b), Numerical investigation of baroclinic instability in the Gaspe current using a frontal geostrophic model, *J. Geophys. Res.*, *104*, 25,685–25,696.
Richards, M. J., M. Wimbush, and L. Mayer (1981), Exceptionally strong near-bottom flows on the continental rise of Nova Scotia, *Science*, *213*, 887–888.
Rossby, C. G. (1940), Planetary flow patterns in the atmosphere, *Q. J. R. Meteorol. Soc.*, *66*, 68–97.
Samelson, R. M., and D. C. Chapman (1995), Evolution of the instability of a mixed-layer front, *J. Geophys. Res.*, *100*, 6743–6759.
Savidge, D. K., and J. M. Bane (1999a), Cyclogenesis in the deep ocean beneath the Gulf Stream: 1. Description, *J. Geophys. Res.*, *104*, 18,111–18,126.
Savidge, D. K., and J. M. Bane (1999b), Cyclogenesis in the deep ocean beneath the Gulf Stream: 2. Dynamics, *J. Geophys. Res.*, *104*, 18,127–18,140.
Shaw, D. (1908), Preface, in *Barometric Gradient and Wind Force*, by E. Gold, Meteorol. Off., H.M. Stationary Off., London.
Shay, T. J., J. M. Bane, D. R. Watts, and K. L. Tracey (1995), Gulf Stream flow field and events near 68°W, *J. Geophys. Res.*, *100*, 22,565–22,589.
Stommel, H. (1965), *The Gulf Stream*, 2nd ed., 248 pp., Univ. of Calif. Press, Berkeley, Calif.
Thomson, R. O. R. Y., and J. R. Luyten (1976), Evidence for bottom-trapped topographic Rossby waves from a single mooring, *Deep Sea Res., Part I*, *23*, 629–635.
Wang, D.-P. (1993), Model of frontogenesis: Subduction and upwelling, *J. Mar. Res.*, *51*, 497–513.
Watts, D. R., K. L. Tracey, J. M. Bane, and T. J. Shay (1995), Gulf Stream path and thermocline structure near 75°W and 68°W, *J. Geophys. Res.*, *100*, 18,291–18,312.
Watts, D. R., X. Qian, and K. L. Tracey (2001), On mapping abyssal current and pressure fields under the meandering Gulf Stream, *J. Atmos. Oceanic Technol.*, *18*, 1052–1067.
Welsh, E. B., N. G. Hogg, and R. M. Hendry (1991), The relationship of low-frequency deep variability near the HEBBLE site to Gulf Stream fluctuations, *Mar. Geol.*, *99*, 303–317.
Woodgate, R. A., and E. Fahrbach (1999), Benthic storms in the Greenland Sea, *Deep Sea Res., Part I*, *46*, 2109–2127.

J. Kämpf, School of Chemistry, Physics and Earth Sciences, Flinders University of South Australia, GPO Box 2100, Adelaide, SA 5001, Australia. (jochen.kaempf@flinders.edu.au)

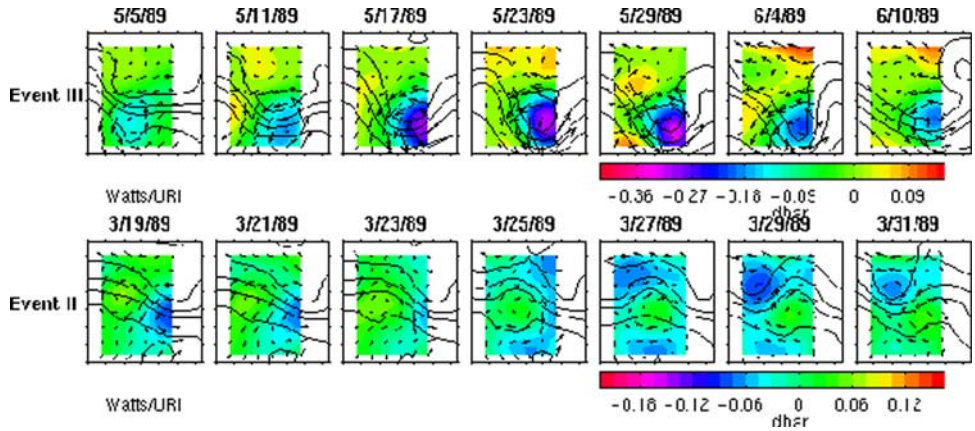

Figure 1. (top) Event III, cyclogenesis at a water depth of ~3.5 km beneath the Gulf Stream. Displayed are lateral distributions of pressure anomalies (shading), currents (arrows; maximum swirl speed ~25 cm/s), and depth contours of the 12°C thermocline (solid lines; CI = 200 m). The Gulf Stream runs from left to right, so that the thermocline depth decreases toward the top in each frame. Each frame covers an area of 200 km × 200 km. (bottom) Event II, development of a weak (swirl speed ~5 cm/s) anticyclone. Courtesy of Randy Watts (2003).